Evolution of the particle size distribution of tricalcium silicate during hydration by synchrotron X-ray nano-tomography

J Neubauer, T Sowoidnich, L Valentini, C Schulbert, C Naber, C Rößler, Julio Da Silva, F Bellmann

Evolution of the particle size distribution of tricalcium silicate during hydration by synchrotron X-ray nano-tomography

J. Neubauer[a*], T. Sowoidnich[b], L. Valentini[c], C. Schulbert[d], C. Naber[a], C. Rößler[b], J. DaSilva[e], F. Bellmann[b]

[a] Friedrich-Alexander Universitaet Erlangen-Nuernberg, GeoZentrum, Mineralogy, Schlossgarten 5a, 91054 Erlangen, Germany

[b] Bauhaus-Universitaet Weimar, Finger-Institute for Building Materials, Coudraystr. 11A, 99423 Weimar, Germany

[c] University of Padua, Department of Geosciences, Via G. Gradenigo 6, 35131 Padua, Italy

[d] GeoZentrum Nordbayern, Section Palaeontology, Friedrich-Alexander Universitaet (FAU) Erlangen-Nuernberg, Loewenichstraße 28, 91054 Erlangen, Germany

[e] European Synchrotron Radiation Facility, 71 avenue des Martyrs, CS 40220, 38043 Grenoble Cedex 9, France

* corresponding author: juergen.neubauer@fau.de

Abstract

The particle size distribution of tricalcium silicate (C_3S) is essential for the modelling of early C_3S hydration kinetics. In this study, this parameter is analysed during the main hydration period until the first 20 h by synchrotron near-field ptychographic (NF-PXCT) and holographic (HXCT) computed nano-tomography. Additionally, X-ray diffraction, ^{29}Si NMR, thermal analysis, scanning electron microscopy, and inductively coupled plasma-optical emission spectroscopy were used to investigate the system evolution. The time-dependent pore solution composition is also provided to gain further information.

HXCT and NF-PXCT show comparable values regarding the evolution of the C_3S particle size distribution during hydration, indicating that C_3S particles smaller than 1.3 µm are completely dissolved after 20 h of hydration. The results can be reasonably reproduced by numerical models if for all particle sizes a constant reacted rim thickness for each degree of hydration is assumed. Data on the aqueous phase composition are also provided.

Keywords

Tricalcium silicate (D); hydration (A); synchrotron nano-tomography (B); near-field ptychography (B); holography (B).

1. Introduction

The hydration of tricalcium silicate (Ca_3SiO_5, C_3S in cement notation) has been investigated in a large number of studies to understand the complex reactions that occur during the hydration of ordinary Portland cement [1]. The products of reaction between C_3S and water (hydration) are C-S-H and portlandite ($Ca(OH)_2$, CH) [1].

The mechanism of C_3S hydration is consistently described as a dissolution-precipitation process with precipitation of C-S-H on the surface of C_3S [2, 3]. Portlandite, in contrast, is formed in the pore space between C_3S particles [4]. Hydration proceeds in stages with different reaction rates called (pre)induction, main hydration period (consisting of acceleration and deceleration) as well as the steady-state period [5]. Beyond this definition, there is no general consensus on the mechanisms governing the kinetics. The present work attempts to provide experimental data for these discussions, particularly on the causes of the deceleration period. A general discussion of C_3S hydration kinetics is not within the scope of this paper but can be found in [2]. To explain the onset of the deceleration period, a limited diffusion of ions from the C_3S surface into the aqueous phase due to covering of the interface by growth of C-S-H [5, 6] has been proposed. In addition, a reduction of the C_3S dissolution rate by consumption of small C_3S grains [1, 7-9] that reduces the overall C_3S reaction rate is discussed as a rate-determining factor during the deceleration period. The main difficulty is the direct experimental observation of C_3S particles during hydration that are overgrown by C-S-H in the presence of portlandite.

Gas adsorption measurements are state-of-the-art for the experimental determination of the specific surface area of anhydrous cementitious materials. Alternatively, the surface area of C_3S can be calculated from the particle size distribution, usually under the assumption that the particles are spheres without consideration of the particle roughness. Laser scattering is commonly applied to determine the particle size distribution of anhydrous cement/C_3S. Because gas adsorption and laser scattering are not phase selective, neither method can be used to measure the C_3S specific surface area of hydrated samples because these contain anhydrous and hydrous phases (C_3S, C-S-H and portlandite).

Imaging techniques such as electron and X-ray microscopy have high potential in the experimental determination of the particle size distribution and thus the specific surface area of C_3S during hydration. This is due to the ability of these methods to identify individual particles in the microstructure. High resolution of scanning electron microscopy (SEM) can be used to record 3D images of cementitious materials using focussed ion beam serial sectioning [10]. The limiting factor is the small size of the analysed volume in the SEM, that is often too small to deduce statistical relevant data for a variety of particle sizes [59, 60, 61]. For X-ray microscopy, one can obtain the absorption and phase-contrast images of the sample for larger volumes. The X-rays attenuated by the sample yield the absorption-contrast, whereas the phase shifts between the incident and the transmitted wavefields, due to the X-rays refraction by the sample, generate phase contrast images [11, 12]. The absorption-contrast imaging of the individual phases, present in low-absorbing materials, consisting of atoms with low atomic number is challenging. In this case, phase-contrast imaging can be used to achieve a high compositional contrast within samples consisting of materials with similar linear attenuation coefficients [13]. However, this property is only accessible by applying imaging techniques using spatially coherent probe beams, such as 3rd-generation-synchrotron radiation

and electron beam or laser, which allows the generation of interference, and by the use of appropriate phase retrieval algorithms.

For high resolution X-ray imaging (2D and 3D), the high brilliance of synchrotron radiation was shown to be advantageous to study multi-hierarchical materials like cement pastes [14] in scattering experiments [15-22] and spectroscopic investigations, both reviewed elsewhere [12, 23-26]. In Holographic X-ray Computed Tomography (HXCT), the detector is placed at 4 different distances from the sample permitting the detection of both the incident and refracted radiation (near-field inline holography). With this setup, the attenuation and the phase shift can be detected. By varying the sample-detector distance, the phase of the wave field can be determined (phase retrieval) solving a mathematically ill-posed problem. The 3D information (tomography) is obtained by rotating the sample and recording images at a series of projection angles for different sample-detector distances [13]. Synchrotron based HXCT was used in several studies dealing with cement. These studies, for example, focussed on the impact of organic admixtures (dispersants or (super)plasticizers) on the formation of C-S-H during the hydration of ordinary Portland cement. The pore size distribution in the hardened samples was also analysed [14, 27].

In Near-Field Ptychographic X-ray Computed Tomography (NF-PXCT), X-ray absorption and X-ray phase-contrast imaging of the samples are obtained also in the holographic regime. The near-field ptychographic approach is based on the acquisition of holograms of the sample at different lateral positions within a structured incoming coherent beam to solve the ill-posed problem in phase-retrieval [53]. With the use of appropriate phase retrieval algorithms, NF-PXCT permits an inherent quantitative 3D imaging of the sample regarding the electron density distribution and by that the mass density at voxel resolution below 20 nm [12, 28, 29]. Far-field Ptychographic X-ray Computed Tomography (FF-PXCT) was, for example, used to determine the mass density of different phases in Portland cement pastes [30-32]. Another study showed the distribution of C_3S, C-S-H, and portlandite in hardened C_3S pastes, proving the strength of the method in phase contrast [11, 31]. The microstructure including AFm, AFt, and aluminium hydroxide was analysed by PXCT in ye'elimite containing materials after hydration [33]. PXCT experiments were also performed with the aim of determining the mass density and to study the reaction of ye'elimite in-situ [34]. Finally, the radius of ettringite needles formed during the hydration of C_3A in the presence of gypsum was investigated by PXCT [35].

Although the experimental determination of the evolution of the particle size distribution of C_3S remains a challenging task, hypotheses were proposed to address this important issue. In the first hypothesis, it is assumed that the degree of hydration of the bulk material is equal to that of the median particle size. Based on this assumption, the median particle radius was used to calculate the reacted rim of C_3S (e), the C-S-H layer thickness (E) and the full particle size (R_P, consisting of a C_3S core overgrown by C-S-H) [36] (abbreviations in Figure 1). The second hypothesis deals with the formation of C-S-H fibres at the surface of C_3S during the acceleration and deceleration period without assuming a diffusion barrier or impingement ('needle model' [2]). Such models may account for a constant C-S-H layer thickness for all particles at a given degree of hydration. The third hypothesis (Figure 1) states that the hydration proceeds faster for small C_3S particles as a result of an identical reacted rim thickness for all particle sizes. This reacted rim thickness increases with hydration progress ('reaction

zone hypothesis') [8]. The assumption of a constant reacted rim thickness was originally developed for the formation of a C-S-H layer around C_3S particles and is used here to describe the thickness of the dissolved layer from the C_3S particles. As a result, smaller particles are fully dissolved earlier than larger particles, and the degree of hydration of the bulk sample is unequally distributed over the different particle size classes. It should be clarified that the first hypothesis mentioned above deals only with the median particle size and not with the full particle size distribution. Furthermore, the calculation of the C_3S particle size distribution during the main hydration period is in principle possible with the 'needle model'. However, the input parameters need to be changed dramatically and are outside the range of reasonable values when this model is used for the present data. For these reasons, only the 'reaction zone hypothesis' is addressed in this work.

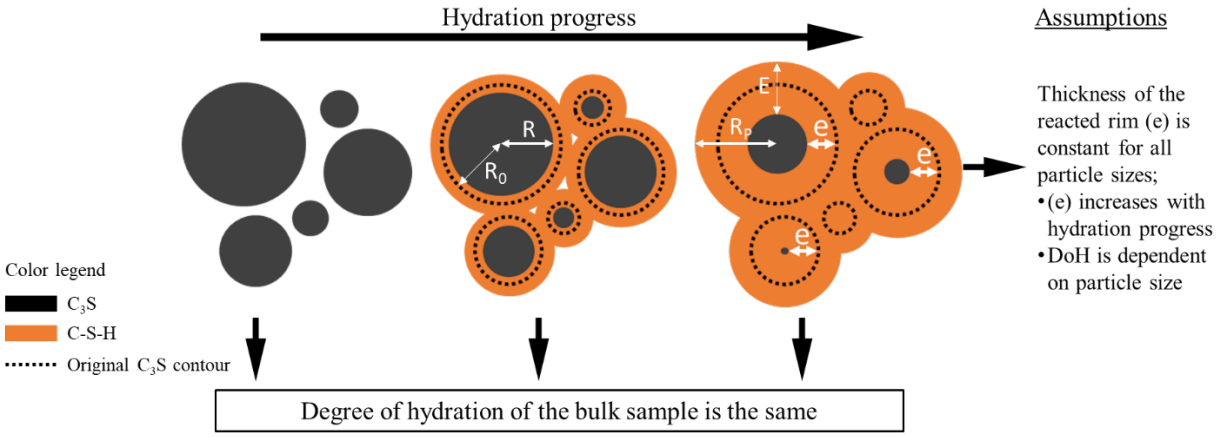

Figure 1: 'Reaction zone hypothesis' for the development of the particle sizes of C_3S during hydration with individual degree of hydration of each particle size due to constant reacted rim thickness. R_0-radius of the anhydrous particle, R-radius of the hydrated particle, e-reacted rim, E-C-S-H layer thickness, R_P-radius of the full particle (C_3S core + C-S-H layer). The presentation focuses on details important to the present study; additional information such as formation of a gap between remaining C_3S cores and C-S-H or the difference between inner and outer C-S-H are not included to increase clarity of the presentation.

The first aim of the present work is to fill the mentioned experimental gaps regarding the measurement of the specific surface area of C_3S during the main hydration period. Therefore, the C_3S particle size distribution is measured by state-of-the-art 3D X-ray nanoimaging technology, uniquely available in 3rd generation synchrotron facilities such as ESRF including the novel near-field ptychographic X-ray computed tomography (NF-PXCT) and holographic X-ray computed tomography (HXCT). The present work is thus the first application of NF-PXCT for characterization of cementitious samples. The used techniques provide an unprecedented high sensitivity to sample morphology and unprecedented high resolution to study dynamics in cement. Thereby, the particle size distribution data are obtained from the analysis of local distribution of the particle morphology by measuring each particle individually.

The second aim of the present work is to evaluate the 'reaction zone hypothesis' by simulation of the development of the C_3S particle size distribution during hydration based on the gathered data. The degree of hydration of C_3S is needed as an input parameter for this purpose, which is independently analysed by X-ray diffraction (XRD), ^{29}Si nuclear magnetic resonance spectroscopy (NMR) and thermal analysis (TA). Additionally, the C-S-H layer thickness at the C_3S surface is evaluated by SEM imaging. The latter approach is complicated by the fact that

SEM is a 2D-method which is discussed in section 3.2. The reliability of the 'reaction zone hypothesis' is explored by comparison of the measured and predicted control parameters: C_3S particle size distribution and specific surface area of C_3S. The aqueous phase composition is measured by means of inductively coupled plasma-optical emission spectroscopy (ICP-OES) during the main hydration period. Combination of the various results allows us to discuss the development of the C_3S particle size distribution during hydration with additional information on the liquid phase composition.

2. Materials and methods

2.1 Raw material preparation and properties

2.1.1 Synthesis of tricalcium silicate

Tricalcium silicate was produced by high temperature solid state reaction from a blend of calcium carbonate (Merck p.a.) and highly dispersed silicon dioxide (Merck p.a.). The raw materials were homogenized and fired at 1520 °C for 8 hours in a platinum crucible and subsequently quenched at 20 °C. This procedure was repeated twice and the material was ground between the high temperature treatments to improve its homogeneity. For high resolution synchrotron X-ray tomography, the volume of the sample has to be very small. To guarantee that a sufficient number of particles are in that volume, the particle size of the C_3S has to be below 10 µm. For this purpose, the material was ground in batches of 25 g for 20 min in a zirconia disk mill at 700 rpm under the addition of 0.08 g diethylene glycol as a grinding aid. The particle size was further reduced in an air classifier to remove particles larger than 10 µm. The individual batches of C_3S were finally homogenized. The particle size distribution measured by Laser scattering is provided in the supplementary information (Figure S1). These results cannot be directly compared to the particle size distribution obtained by X-ray tomography as both methods are based on different physical methods and use different definitions to extract the particle size from the experimental data.

The C_3S produced in this study has the following chemical composition (determined by chemical wet analysis based on titration of calcium , gravimetric determination of silicon as well as ICP-OES analysis for all other elements except silicon): 72.8 wt.-% CaO, 26.1 wt.-% SiO_2 and 1.0 wt.-% LOI, whereas the concentration of foreign oxides was below the limit of detection (0.1 wt.-%). The free lime concentration determined by Franke-method [37] was 0.3 wt.-%. Analysis by QXRD indicated the presence of pure C_3S in the triclinic modification and the concentration of belite and free lime were below the limit of quantification (LOQ: 5 wt.-% for belite and 0.5 wt.-% for CaO).

2.1.2 Hydration of C_3S

All experiments were designed to match the requirements of synchrotron X-ray nano-tomography. As stated before, particle sizes below 10 µm are specifically prepared in order to increase the spatial resolution of the tomography. Therefore, a relatively high water/C_3S-ratio (by mass) of 3.0 was required to produce a workable suspension as the surface area of the

starting material is very high. This water/solid-ratio is higher than normally used for hydration studies on pastes but it was recently confirmed that hydration kinetics of C_3S are not affected by the water/solid-ratio [58]. Accordingly, 15 g of C_3S was mixed with 45 g filtered saturated calcium hydroxide solution and 0.10 g superplasticizer. Superplasticizer (SP1 from reference [38]) was added to the starting solution prior to mixing to avoid the formation of agglomerates due to the surface charge of the C_3S particles [39, 40]. This superplasticizer is a methacrylic acid-co-polyethylene glycol type polycarboxylate with the following parameters: 8.2 repeating units, 3.9 monomers per repeating unit, 23 monomers in the side chain with a total molecular weight of 10,930 g/mol.

The closed vessel filled with the suspension was stirred for 24 hours at a temperature of 25 °C. Samples (approx. 6 ml suspension) taken after 4, 8, 12, and 16 hours of hydration were filtered in a gaseous nitrogen pressure filtration unit using filters with a pore width of 15 nm. This relatively small pore width of the filter was used to avoid C-S-H particles from passing through the filter, especially when superplasticizers are present [38]. As a consequence, the filtration process took 30-45 min at a pressure of approx. 2 bar. The solid residue of the filtration was dried at 60 °C for X-ray nano-tomography, QXRD, ^{29}Si-NMR, SEM, and thermal analysis. It was not possible to extract pore solution after 20 and 24 hours by this method. Additional samples (< 100 mg) were taken after 6, 10, 14, 18, and 22 hours only for thermal analysis by drying at 60 °C without prior filtration.

2.1.3 Preparation of the hydrated C_3S samples for Scanning Electron Microscopy (SEM)

Sample preparation for SEM characterisation included embedding of the hydrated samples in epoxy resin and mechanical polishing using diamond slurries of 15, 9, 3, and 1 µm particle size. The polished samples were coated with gold to ensure electric conductivity of the sample surface.

2.1.4 Preparation of the hydrated C_3S samples for synchrotron X-Ray nano-tomography

The samples for synchrotron X-ray nano-tomography were produced by embedding the samples in a commercial two-component epoxy resin. Thin filaments composed of epoxy resin and sample material were pulled while the epoxy-C_3S mix was already stiff but still workable. After hardening of these filaments containing the samples embedded in epoxy resin, these were cut into small segments with a length of 1-2 mm. Segments with a diameter of approximately 100 µm were selected under an optical microscope and glued to the sample post of the device by epoxy resin. Thus, the final length of the filaments was approximately 1 mm and the diameter was approximately 100 µm. Only the anhydrous C_3S was mixed with a highly adsorbing polymer before embedding in resin as described before. This was done to produce an organic film on the surface that enables the observation of individual C_3S particles instead of agglomerates. For this purpose, 1.00 g C_3S was mixed with 2.00 g polymer dispersion (styrene-acrylate co-polymer model latex in [41]) and treated by ultrasound (frequency: 20 kHz, amplitude 43 mm) for 20 seconds and quickly dried after 1 minute at 50 °C to avoid a reaction with water. A schematic illustration of the sample preparation steps and the nano-tomography as well as simulation is provided in the supplementary information (Figure S2).

2.2 Analytical methods

2.2.1 Degree of hydration of C_3S and aqueous phase composition during hydration

X-ray diffraction

XRD patterns of the hydrated samples were obtained in a D8 Advance diffractometer (BRUKER-AXS) equipped with a LynxEye detector using a Cu-tube operating at 40 mA and 40 kV. The scans from 7 to 70 °2θ were recorded with a step size of 0.011 °2θ and a counting time of 0.5 seconds per step. The concentration of individual phases was calculated using the Rietveld-software Topas 5.0 (BRUKER-AXS), using a recently developed external standard method [42, 43]. The respective crystal structures were applied to describe the tricalcium silicate [44] and portlandite [45] contribution to the diffraction pattern, while a PONKCS approach by Bergold et al. [46] was employed to describe the C-S-H contribution. The amorphous content in the anhydrous tricalcium silicate was not increased by the intense milling.

Thermal analysis (TA)

Thermogravimetry data were obtained in a TA instruments SDT Q600 device at a heating rate of 10 K/min under a stream of nitrogen. The water content of C-S-H was determined by subtraction of the change in mass related to dehydration of portlandite and the decarbonation of calcium carbonate from the loss on ignition at the final temperature (1000 °C). It was revealed in this calculation that the C-S-H of the hydrated C_3S sample contains 2.6 moles of water. Under the assumption of a Ca/Si molar ratio of 1.7 for C-S-H, the hydration reaction of C_3S can be written as:

$$C_3S + 3.9\,H \rightarrow C_{1.7}SH_{2.6} + 1.3\,CH \qquad \text{Equation 1}$$

Equation 1 was used for the calculation of the C_3S content in the hydrated samples.

^{29}Si-NMR spectroscopy

^{29}Si solid-state magic angle spinning (MAS) nuclear magnetic resonance (NMR) spectroscopy was performed in a spectrometer equipped with an Oxford wide bore magnet (11.7 T), a Bruker Avance III 500 console and a Doty triple resonance probehead for 7 mm (O.D.) zirconia rotors.

Single-pulse and cross-polarization (^{29}Si{^{1}H} CP) experiments were conducted by ^{29}Si solid-state NMR to quantify the concentrations of C_3S, C-S-H and metastable hydrate phase [47], which can be interpreted as a first form of C-S-H [48]. The single-pulse experiments used a MAS spinning rate of 4 kHz, a $\pi/2$ pulse length of 6.4 µs, 128 scans, and a recycle delay time of 600 s. This recycle delay time is too short for complete relaxation of the silicon sites in C_3S resulting in an underestimation of the intensity of this phase compared to C-S-H which has a much lower relaxation time. Thus, the intensities extracted from the deconvolution need to be multiplied by a factor of 3.62, which was obtained by comparing a fully relaxed spectrum (recycle delay time 4 hours, 24 scans) with a spectrum acquired at the same degree of relaxation (recycle delay time 600 s, 24 scans) as the samples used for quantitative analysis. The chemical shifts associated to the different phases and the recorded spectra obtained by the single-pulse experiments are provided in the supplementary information (Figure S3).

The $^{29}Si\{^{1}H\}$ CP experiments were conducted using parameters that were adjusted using a sample of α-C_2SH at the same MAS frequency of 4 kHz. The spectra were recorded using an initial ^{1}H pulse (π/2 pulse length of 4.5 µs), a contact time of 4 ms with a ^{1}H rf field strength of 38.3 kHz (ramp 10090) and a ^{29}Si rf field strength of 30.9 kHz, ^{1}H decoupling during acquisition for 10 ms, a recycle delay time of 3 s and 1024 scans.

The concentration of C_3S, C-S-H, and a metastable hydration product containing Q^0 sites was computed from the (corrected) relative intensities from the deconvolution of the spectra, the silicon concentration in the sample and the molar weight of the phases. The molar weight of C-S-H and the metastable hydration product is based on the composition of these phases assuming 1.7 $CaO \cdot SiO_2 \cdot 2.6\ H_2O$ and 1.3 $CaO \cdot SiO_2 \cdot 2H_2O$ [48], respectively.

All chemical shift data are reported relative to tetramethylsilane (TMS) as an external standard. The software DMFit was used for the deconvolution of the spectra [49].

The $^{29}Si\{^{1}H\}$ MAS NMR (CP) spectra and the chemical shifts of the phases are presented in the supplementary information of this article (Figure S4 & S5, Table S2).

ICP-OES

Ion concentrations in the filtered aqueous solutions were analysed by ICP-OES using a Horiba Jobin Yvon, active M with radial observation. Calcium and silicon concentrations were measured at a wavelength of 373.69 nm and 251.61 nm, respectively. The aqueous phase was obtained by filtration of the suspensions after 4 h, 8 h, 12 h, and 16 h of hydration. The filtered solutions were diluted and stabilized by the addition of 0.2 g of 5 M HNO_3 for analysis by means of ICP-OES. This dilution was taken into account.

2.2.2 C-S-H layer analysis by means of Scanning Electron Microscopy (SEM)

Microstructural characterisation was carried out using a SEM equipped with a field emission gun (Nova NanoSEM 230 FEI). For the detection of backscatter electron images, 12 kV acceleration voltage and 1.8 nA probe current were used (high vacuum mode of the instrument). The C-S-H layer thickness was measured by manually selecting undisturbed (by sample preparation and vacuum) hydration rims. For each sample more than 50 particles have been analysed. It is known that C-S-H can lose water when exposed to high vacuum but it is not expected that the morphology is significantly affected by this dehydration (measurements were taken in areas were no significant shrinkage cracking was observed).

2.2.3 C_3S particle size distribution during hydration by holo- and near-field ptychographic nano-tomography using synchrotron radiation

The experiments were carried out at the ID16A nano-imaging beamline of the European Synchrotron Radiation Facility (ESRF) [50]. This end-station is optimized for efficient hard X-ray nano-focusing and designed to provide coherent X-rays for nanoimaging. During the experiments, the sample was exposed to vacuum (around 10^{-7} mbar) at room temperature. However, the C_3S and C-S-H particles are not directly exposed to the vacuum and subsequent water loss as the material is fully enclosed in epoxy resin. The beamline offers a piezo-driven short-range hexapod stage for the accurate positioning and scanning of the sample under the control of capacitive sensors. Two sets of tomographic experiments were conducted, namely,

HXCT and NF-PXCT. Details of the experiments using those two techniques are given in the supplementary information of this article.

3. Results

3.1 Degree of hydration of C_3S and aqueous phase composition during hydration

The samples obtained during the hydration experiment were analysed by three independent methods to determine the degree of hydration. These include QXRD, ^{29}Si MAS NMR spectroscopy, and thermal analysis. The degree of hydration is calculated from the evolution of the concentration of tricalcium silicate in the samples when using QXRD and ^{29}Si NMR. In contrast, the C_3S concentration is indirectly assessed by thermal analysis by using the determined concentrations of C-S-H and portlandite to stoichiometrically calculate the C_3S concentration (equation 1). The concentration of C_3S during hydration is plotted in Figure 2 as the mean value, with the corresponding standard deviation obtained from the individual methods. A method-dependent list of these results is provided in the supplementary information of this article (Table S1). The mean value of the C_3S concentration against time is fitted using Equation 2:

$$C_3S\ [wt.-\%] = A2 + \frac{(A1-A2)}{1+e^{\frac{t-t0}{dt}}} \qquad \text{Equation 2}$$

A corrected $R^2 = 0.99955$ was achieved with the fit parameters A1 = 97.6 wt.-%, A2 = 19.5 wt.-%, t0 = 12.9 h and dt =2.1 h. This mathematical fit is also given in Figure 2 (dotted line). The first derivative of this fit corresponds to the reaction rate and is plotted on the right axis of Figure 2. The application of reaction calorimetry that is generally used for the determination of the hydration rate [1] was not possible because the hydration was performed in suspensions (water/C_3S - ratio (by mass) of 3.0) and thus continuous stirring is needed during the measurement.

As shown in Figure 2, the concentration of C_3S at the start of the experiment is slightly lower than 100 wt.-%. This can be the consequence of the adsorption of a small amount of water in the air classifier during milling or other procedures. Between 5 and 20 h, the concentration of C_3S drops to a final value of 19 wt.-% as it is consumed during the main hydration period. Such a high degree of reaction (0.81) is attributed to the very small particle sizes of the used C_3S powder. The maximum rate of reaction during the main hydration period is observed after approximately 13 hours. This is relatively late when compared to other studies using pure tricalcium silicate and the shift of the maximum of the main hydration peak is connected to the addition of superplasticizer that is known to retard the nucleation and growth of C-S-H. However, the retarding effect is relatively low as the concentration of superplasticizer was only 0.67% relative to C_3S. Between 20 and 24 hours, the concentration of C_3S decreases from

23 to 19 wt.-%, indicating that the reaction has slowed down and the main hydration period has ended.

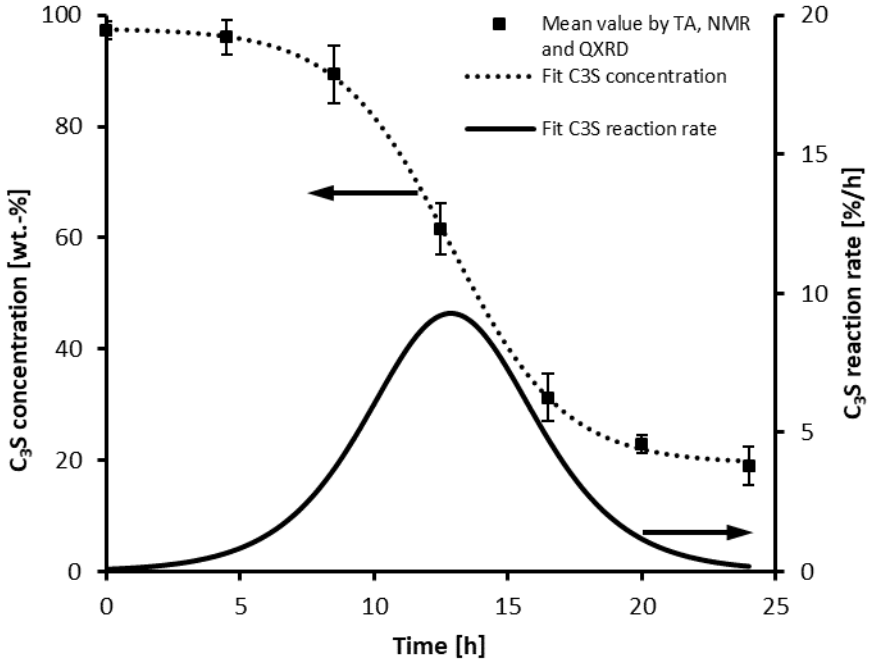

Figure 2: C_3S concentration during 24 h of hydration given as the mean value from TA, NMR, and QXRD measurements (black squares) with its mathematical fit by Equation 2 (dotted line), and C_3S reaction rate as the first derivative (multiplied by -1) of the C_3S concentration fit (bold line, right hand axis).

In addition to the C_3S concentration, the aqueous phase of the C_3S suspensions during hydration was analysed by ICP-OES (Table 1). The results show that the calcium ion concentration is already at a very high level after 4 hours hydration (32 mmol/L) and increases after 8 h to 34 mmol/L. At later hydration times, the calcium ion concentration in the aqueous phase decreases, which can be attributed to nucleation and growth of portlandite [51]. A calcium ion concentration of 28 mmol/L was observed after 16 hours reaction. The silicon concentration displays an opposite trend compared to the calcium ion concentration, decreasing from 20 to 16 µmol/L between 4 and 8 hours. A slight increase in silicon is observed after 12 hours, followed again by a decrease after 16 hours. A possible explanation of the observed trends in the ion concentrations of the aqueous phase can be deduced from the plot of Si against Ca (Figure S7, supplementary information). In this way the results can be interpreted that the aqueous phase is close to an equilibrium with a metastable C-S-H [48] for hydration periods up to 12 h and departs towards stable C-S-H [52] at later hydration times.

3.2 C-S-H layer analysis by means of SEM

The hydrated samples were investigated by SEM with the aim of evaluating the C_3S particle size distribution and the C-S-H layer thickness at the surface of the C_3S particles during hydration. Figure 3 shows examples of these SEM investigations.

The dark areas in the SEM images shown in Figure 3 represent the epoxy resin, which was used to fix the material. The C_3S particles are light grey, C-S-H is slightly darker covering the C_3S surface. Portlandite can be recognised by its shape, i.e., as elongated shapes resulting from sectioned plate-like crystals. Mean values of the C-S-H layer thickness were estimated for a

number of 57 (12 h), 77 (16 h), and 70 (20 h) C_3S particles providing the sum of inner and outer C-S-H. These analyses provide only semi-quantitative information as the polishing process during sample preparation cuts the particles not through the volume centre. An extraction of the true thickness of the C-S-H layer from these results is not straightforward and requires a number of assumptions for particle shape and other properties [54]. It is also complicated by the fact that the C_3S particles have irregular shapes and there is a high variation in the thickness of the C-S-H layer even at the same grain. Thus, an evaluation of accurate quantitative information is complicated but a semi-quantitative approach demonstrates a growing thickness of the C-S-H layer around tricalcium silicate during hydration as predicted by the reaction zone hypothesis in Figure 1. Image analysis of the sample hydrated for 12 h shows that the C-S-H covering the C_3S particles has the lowest thickness of the investigated samples with a value of 300 ± 80 nm. This C-S-H layer thickness increases after 16 h of hydration to a mean value of 670 ± 170 nm and after 20 h of hydration to 800 ± 260 nm. Although these results bear a large error, the conducted SEM investigations prove the findings [4, 53] that the C-S-H layer thickness increases with increasing hydration time. The values obtained for the C-S-H layer thickness are much higher than the C-S-H needle length results summarized in [2] but in broad agreement with layer thicknesses expected from BNG simulations [8]. The deviation from values reported in [2] may be due to the fact that the C_3S used in this study had a higher surface area, which resulted in a higher degree of hydration which facilitates formation of longer C-S-H needles. It was also attempted to extract the particle size distribution of tricalcium silicate from the SEM micrographs. These efforts have indicated that the size of the C_3S cross sections can be analysed accurately by SEM but a recalculation of the diameter of the 3D-particles from the 2D cross sections is challenging due to irregular shaped alite cores. In addition to C_3S and C-S-H, also portlandite particles are observed in all samples, especially in the 20 h sample.

A)

B)

C)

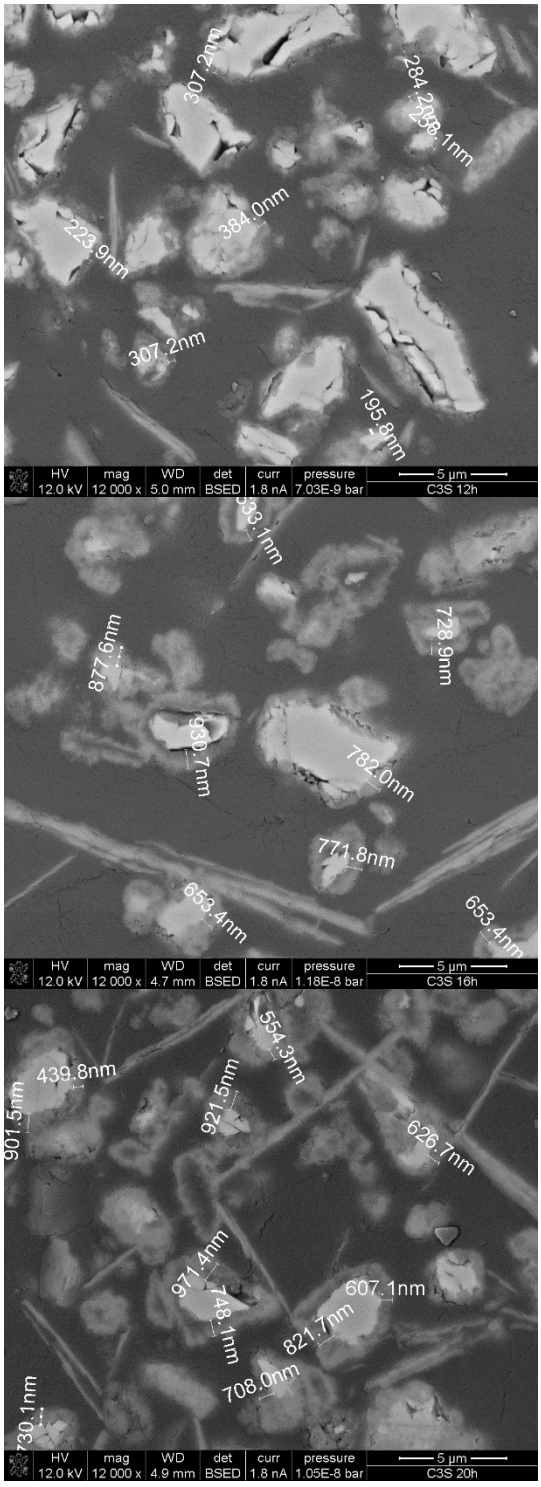

Figure 3: SEM images of embedded samples hydrated for 12 h (A), 16 h (B), and 20 h (C) with measurements of the C-S-H layer thickness.

3.3 C_3S particle size distribution during hydration by holo- and near-field ptychographic tomography using synchrotron radiation

The first step in determining the particle size distribution of C_3S during hydration is the identification of the C_3S particles in the samples. Figure 4 provides a greyscale image from the HXCT (left hand) together with the processed binary image obtained by the used segmentation algorithm (right hand) [55]. It can be seen that the used segmentation algorithm showed a good performance in separating neighbouring particles and removing hydration products.

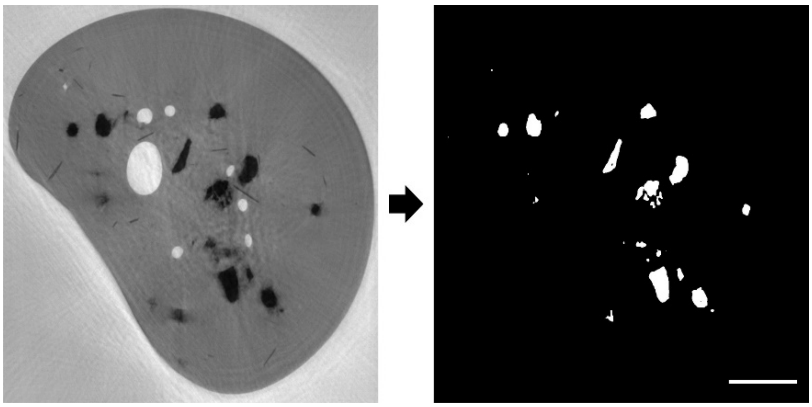

Figure 4: Grayscale (left) and binary (right) images relative to a 2D section through the reconstructed volume (12-hours hydrated sample). Black: cement particles; grey: glue; white: air voids. Segmented C_3S particles in the binary image are shown in white. Scale bar: 10 µm.

The image processing from the NF-PXCT experiments is exemplarily shown in Figure 5 for the sample hydrated for 12 h. The C_3S particles appear in light grey, whereas C-S-H and portlandite are dark grey and the resin still darker. Air bubbles are black spheres. The hydration products C-S-H and portlandite have almost the same grey-level but a different morphology as calcium hydroxide forms elongated particles of several micrometers in the longest dimension. Figure 5 shows that the C_3S particles are clearly identified as their grey level is different from all other phases in the analysed volume. These differences in grey level between C_3S and the other phases allow an extraction of the particle size distribution of tricalcium silicate. A related analysis of the C-S-H shell thickness is complicated by the fact that the grey levels of C-S-H and portlandite are almost identical. The processed images were segmented to identify the phase present in the individual voxel from the grey level. A minimum of 8 connected voxels representing tricalcium silicate was considered as the smallest particle size which could be identified in the segmentation process. These 8-voxel clusters at an individual voxel size of 50 nm reveal the volume of the smallest particles which is 10^6 nm^3. The diameter of a sphere with the identical volume is 124 nm. All particle diameters determined from nano-tomography data which are presented in the following sections are calculated as spheres with identical volume compared to the analysed volume of the irregular shaped particles.

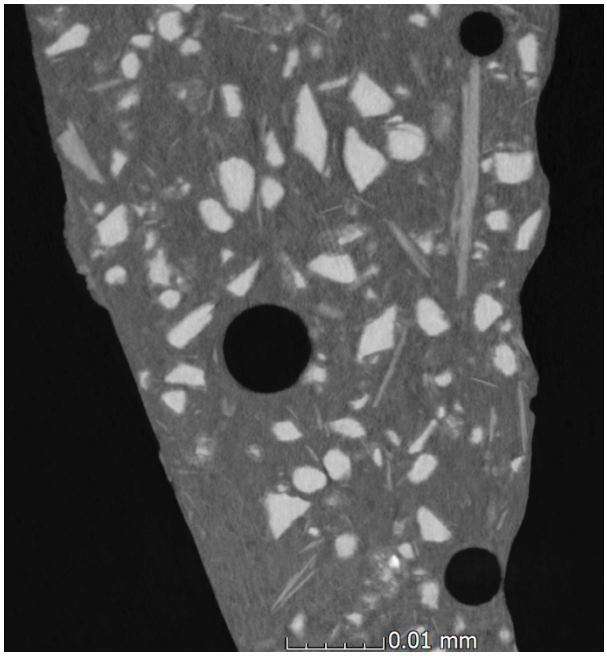

452

453 Figure 5: 2D view of the C_3S sample hydrated for 12 h showing irregular shaped C_3S particles, elongated portlandite
454 sections, C-S-H as a hydration rim around tricalcium silicate, epoxy resin and air (black).

455 In the following, the identified C_3S particles were converted into particle size distributions.
456 The volume distributions of the anhydrous C_3S particles are shown in Figure 6 obtained by
457 HXCT and NF-PXCT.

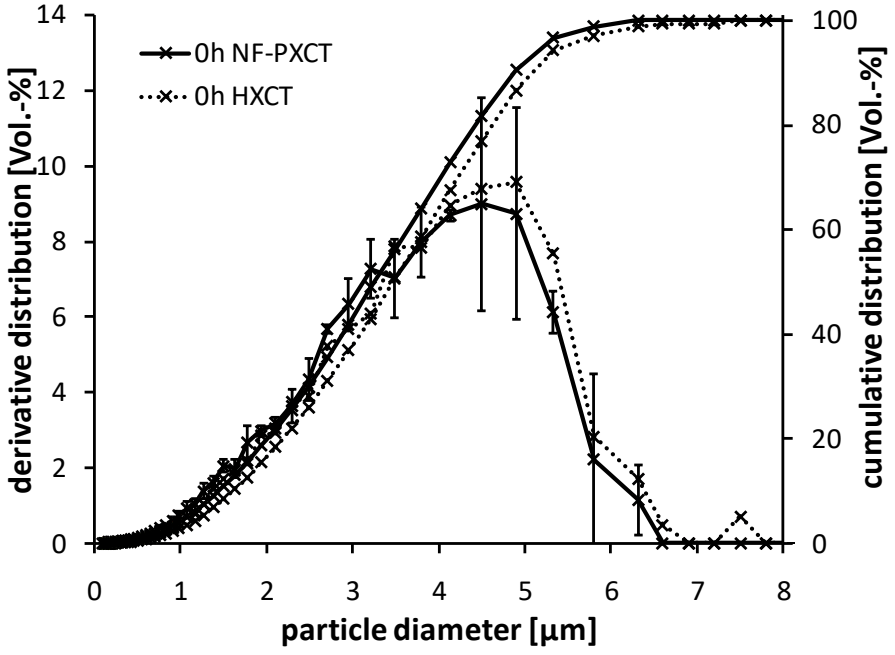

458

Figure 6: Volume-based particle size distribution (cumulative and derivative) for HXCT and NF-PXCT measurements of anhydrous C_3S.

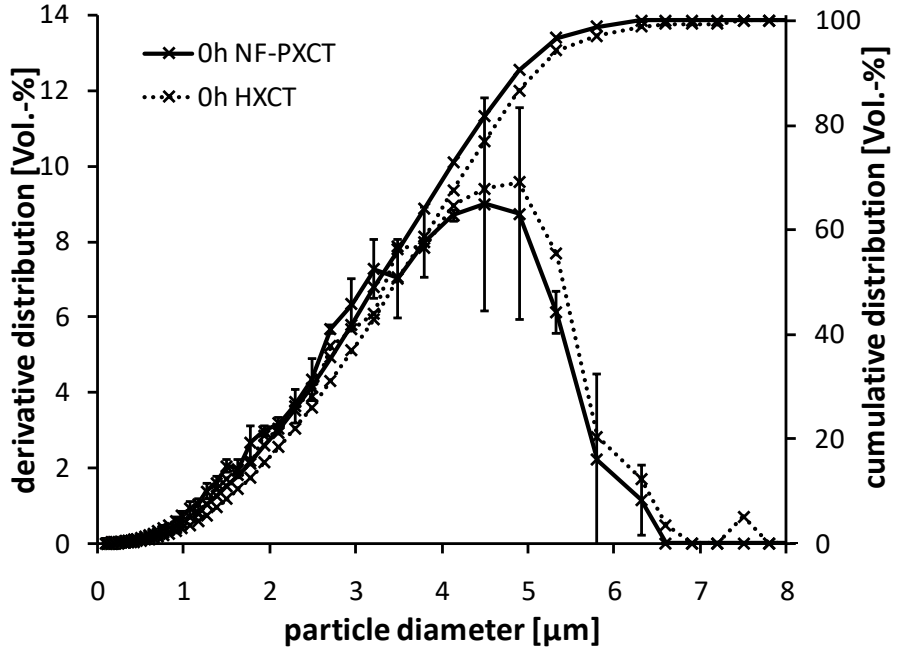

Figure 6 shows that NF-PXCT and HXCT give comparable results for the volume-based particle size distribution of the anhydrous C_3S. The maximum C_3S particle diameter is 6.3 µm (NF-PXCT) and the smallest measures 124 nm as defined during the post-processing procedure (minimum 8 voxels per particle are selected to avoid any possible contamination of the dataset due to the presence of noise). The HXCT results show some variation in grey level intensity complicating the segmentation process. It appears from the HXCT data that a 7.5 µm particle is present in the analysed volume which is not identified by NF-PXCT. A closer comparison of the tomographic data reveals that such a particle is not present but consists of an agglomeration of two particles in the HXCT reconstruction. This confirms the improved resolution and an enhancement in grey-level contrast of the NF-PXCT results compared to HXCT.

Results in Figure 7 show that the maximum particle size is reduced from 6.3 µm in the anhydrous sample to 5.5 µm (NF-PXCT) or 5.9 µm (HXCT) after 12 h of hydration. The same agreement between NF-PXCT and HXCT is observed for the other samples. The data also reveal a further decrease of the maximum particle size to 5.4 µm (NF-PXCT) or 5.1 µm (HXCT) after 16 h of hydration and the maximum particle size is 4.8 µm (NF-PXCT and HXCT) after 20 h of hydration. This implies that the impact of hydration is clearly visible by a reduced diameter of the largest particles. The situation is different for small particles sizes as the number of particles in a given size class is reduced by dissolution of initially anhydrous particles and increased by size reduction of particles of initially larger particles during hydration. Overall, for the observed hydration periods, both effects lead to steeper and narrower particle size distribution as shown in Figure 7. The qualitative trend to smaller particles sizes during hydration observed for the largest particles is not evident in all size classes for all hydration times. Unexpectedly, the relative concentration of medium sized particles is higher in the 20 hours sample than in the 16 hours sample.

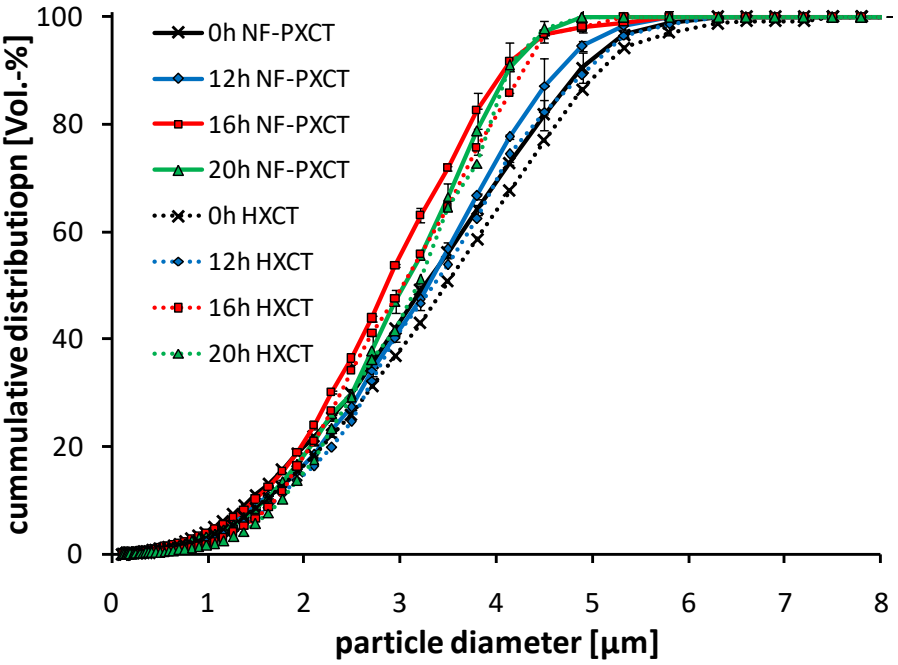

Figure 7: Volume-based cumulative particle size distribution obtained from NF-PXCT and HXCT measurements of C_3S.

4. Discussion

A hydration time dependent particle size distribution measurement during C_3S hydration with full phase selectivity was achieved in this study by employing synchrotron X-ray nano-tomography. As mentioned in the introduction, this experimental data was unavailable up to now for a description of the C_3S hydration. The obtained data on the development of the particle size distribution are used to evaluate the 'reaction zone hypothesis'. This hypothesis claims that the hydration proceeds in an identical reacted depth (rim) for all sizes of particles (Figure 1). This reacted rim increases with the degree of hydration. The mathematical expressions are developed in the following equations.

4.1 Mathematical expression

With the reacted rim thickness e (Figure 1) and the initial diameter of particles of class i (denoted $D_i(0)$), the diameter of the particle of class i at distinct degree of hydration $D_i(\alpha)$ is:

$$D_i(\alpha) = D_i(0) - 2e \qquad \text{Equation 3}$$

With:

$$2e \leq D_i(0) \qquad \text{Equation 4}$$

From $D_i(\alpha)$, the mass of particle of class i(m_i) can be calculated using the corresponding volume of a sphere and the mass density of C_3S (3.16 g/cm³). The degree of hydration of particle of class i at time t, $\alpha_i(t)$, reads:

$$\alpha_i(t) = 1 - \frac{m_i(t)}{m_{i,0}} \qquad \text{Equation 5}$$

With $m_i(t)$ and $m_{i,0}$ being the mass of the particle i at time t and at time zero, respectively.

The sum over all particles classes i weighted by the number of particles in each class N_i of the initial bulk sample gives the degree of hydration of the bulk sample α(t):

$$\alpha(t) = 1 - \sum_{i=1}^{n} \frac{\sum_i^n m_i(t) N_i}{\sum_i^n m_{i,0} N_i} \qquad \text{Equation 6}$$

During simulation, the reacted rim thickness e is iterated until the global degree of hydration of the particles matches the measured degree of hydration at time t of the bulk sample (α(t), eq. 6, depicted in Figure 2). The result of this simulation gives the reacted rim thickness e and the degree of hydration distributed over all particle sizes.

4.2 Application

For the following simulation, the measured particle size distribution (NF-PXCT only) of the reference sample and the degree of hydration of the bulk samples are used as input parameters. Figure 8A shows the degree of hydration of the bulk samples distributed over all C_3S particle sizes calculated from eq. 5 for the samples hydrated for 12 h, 16 h, and 20 h. In Figure 8B, the corresponding reacted rim thickness 'e' is presented.

The simulation in Figure 8A shows that the C_3S particles with diameter smaller than 0.42 µm have completely reacted after 12 h of hydration. The degree of hydration of particles with diameter ranging from 0.40 µm to 6.31 µm decreases from 1.0 to 0.2 non-linearly. After 16 h of hydration, particles smaller than 0.98 µm have completely reacted and after 20 h this value is 1.22 µm. The simulated values for the distribution of the degree of hydration over the initial particle sizes (Figure 8A) correspond at the same time to the reacted rim thickness, which is depicted in Figure 8B. It can be seen that the reacted rim increases non-linearly with increasing degree of hydration.

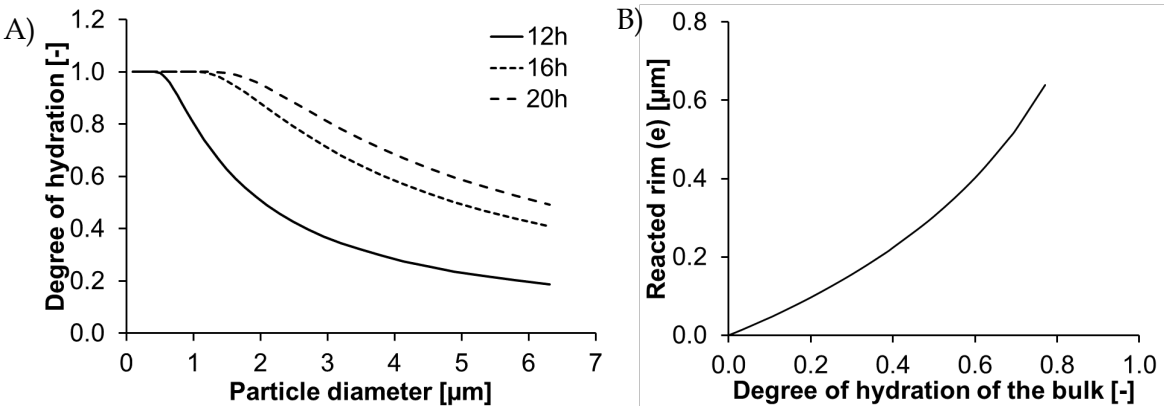

Figure 8: Simulated degree of hydration of the C_3S particles in dependence of their size after 12 h, 16 h, and 20 h of hydration (A). Calculated reacted rim thickness of the C_3S particles in dependence on the degree of hydration (B).

4.3 Evaluation

The 'reaction zone hypothesis' is qualitatively evaluated by comparing the measured values of the C-S-H layer thickness and the particle size distribution in the following. A quantitative evaluation will be presented afterwards by the comparison of the measured and predicted specific surface area of C_3S during hydration.

4.3.1 Qualitative evaluation of the simulation

The qualitative evaluation step regarding the simulation based on the 'reaction zone hypothesis' centres around the comparison of the predicted and measured particle size distribution of C_3S during hydration. In addition to the particle size distribution of the starting material (measured by NF-PXCT), also the degree of hydration of the samples is taken into account as an input parameter. From this, the volume fractions of C_3S in the size classes i can be calculated for the hydrated samples. The results of this calculation are compared to the measured values in Figure 9.

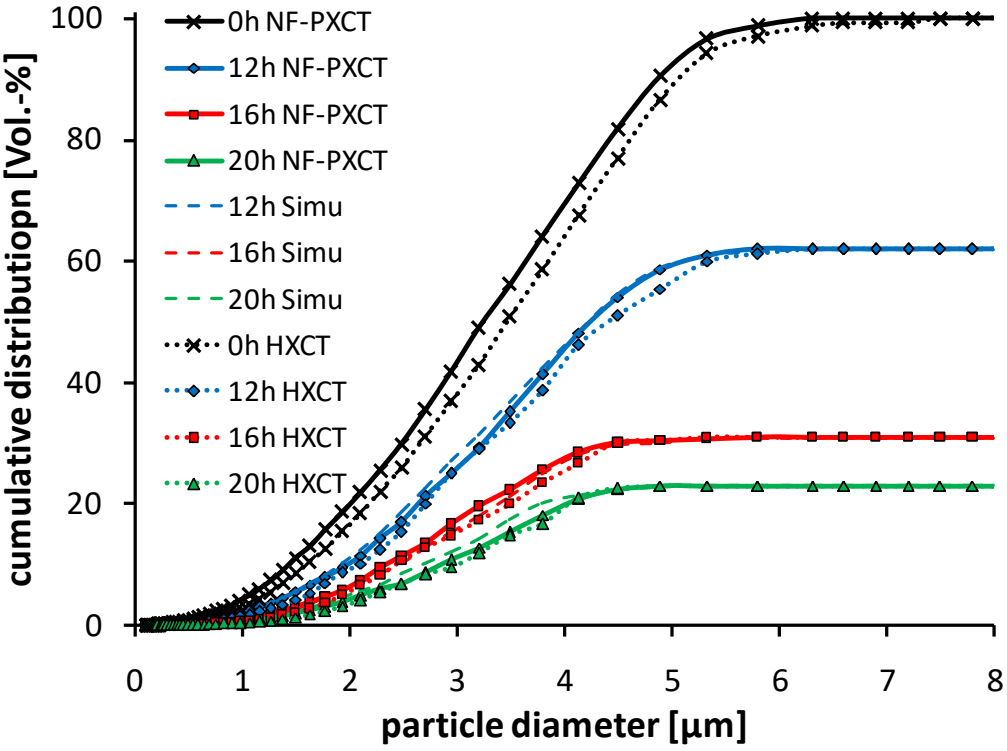

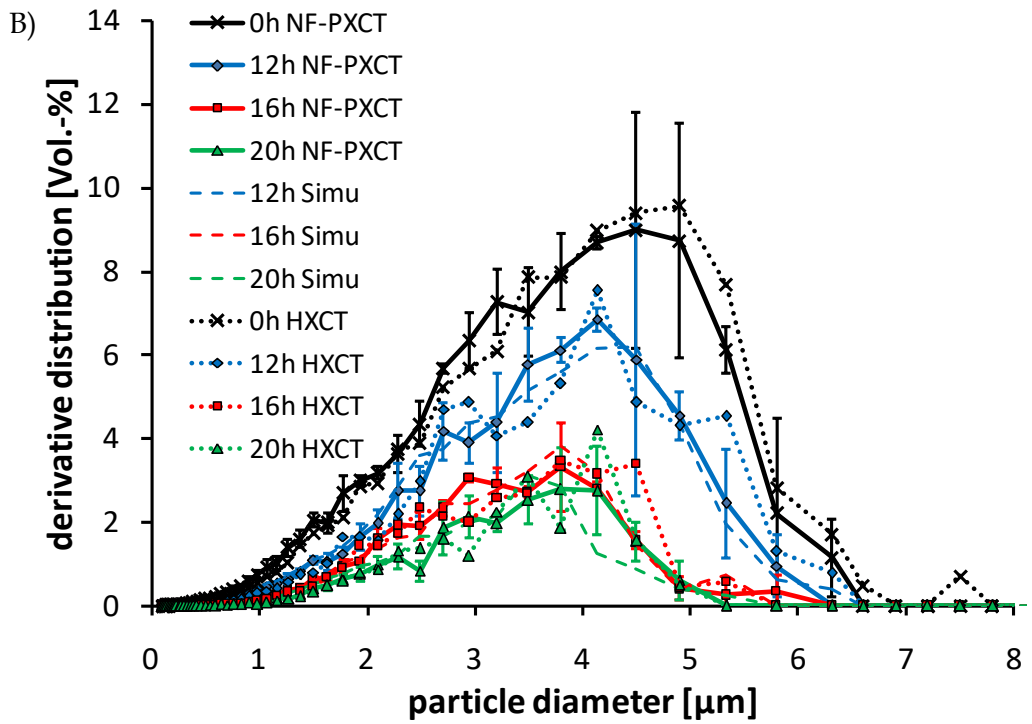

549 Figure 9: Particle size distribution (A: cumulative, B: derivative) during C_3S-hydration. Measurement (NF-PXCT,
550 HXCT) and simulation.

551 The results from the simulation and nano-tomography are displayed in Figure 9. The
552 simulation results are obtained using the particle size distribution from NF-PXCT, degrees of
553 hydration from section 3.1 and the shrinking core model from section 4.1. A close agreement
554 between the particle size distributions from simulation and nano-tomography is indicated by
555 the cumulative curves (Figure 9A) and impressively confirmed by the differential curves
556 (Figure 9B). The error bars in that Figure refer to the standard deviation (1σ) of the NF-PXCT
557 results that was obtained by splitting the analysed volume in three sub-volumes followed by
558 extraction of the particles size distribution for each sub-volume. Thus, the standard deviation
559 is a conservative approximation for the uncertainties introduced by particle statistics.

560 It is evident from Figure 9B that the simulation and the experimental results agree closely and
561 always within the standard deviation. The quality of the results is underpinned by the fact that
562 the curves referring to the individual hydration times are distinct from each other and fall
563 outside the standard deviation from the other hydration times. Only in the late stage of
564 hydration when the reaction slows down, the particles size distributions are located within the
565 standard deviation of the curve from another hydration time (16 h and 20 h samples), see
566 Figure 9B.

567 It is important to point out that the simulation data obtained from the shrinking core model
568 closely agrees with the experimental data thus confirming the validity of that model - at least
569 for the samples analysed in this study.

570 **4.3.2 Quantitative evaluation of the simulation**

571 The qualitative evaluation of the 'reaction zone hypothesis' shown in section 4.3.1 is now
572 followed by quantitative tests by analysing the surface area of C_3S during hydration (Table 1).
573 A comparison of measurements and predictions show that the surface area of C_3S decreases

574 during hydration. A close agreement between both nano-tomography techniques and the
575 simulation is observed. The maximum deviation between different techniques was as small as
576 0.06 m²/g (NF-PXCT versus HXCT for the anhydrous C_3S). This difference is due to difficulties
577 in the segmentation of the HXCT-data of this sample already noted in section 3.3. The absolute
578 differences between the methods are even smaller for all other samples with HXCT tending to
579 give slightly lower values. The good agreement between simulation and experimental data
580 implies that the 'reaction zone hypothesis' can predict the specific surface area of tricalcium
581 silicate during hydration with high accuracy. This statement applies to the samples prepared
582 in this study and a general validation of the model would require a systematic analysis of
583 many other samples.

584 The surface area data in Table 1 refers to the outer surface of the particles and may be modified
585 by changes in micro-roughness of the particles during hydration. It has to be kept in mind that
586 the values reported in Table 1 account for particles larger than 124 nm as smaller particles
587 cannot be detected by the experimental methods used in this study. The presence of smaller
588 particles will lead to higher surface areas and can be included in the simulation. Such particles
589 smaller than 124 nm had to be removed from the present simulation to be consistent with the
590 experimental study. A repetition of the simulation using the particle size distribution from the
591 laser diffraction data would derive surface area data that is systematically higher than the
592 results in Table 1. This difference is due to the fact that laser diffraction can analyse much
593 smaller samples as it operates on a different physical basis. Such data was not included in the
594 current study as it cannot be compared to the experimental results obtained by nano-
595 tomography.

596

Hydration time	Degree of hydration	Aqueous phase composition		Surface area C_3S with respect to 1 g alite [m²]		
[h]	[-]	Ca [mmol/L]	Si [µmol/L]	Ptycho-graphy	Holo-graphy	Simu-lation
0	0.03	-	-	0.72	0.66	-
4	0.04	19.8	32.1	-	-	0.66
8	0.11	15.6	33.6	-	-	0.62
12	0.38	17.2	32.6	0.43	0.40	0.43
16	0.69	15.5	28.2	0.24	0.21	0.22
20	0.77	-	-	0.17	0.15	0.17
24	0.81	-	-	-	-	0.14

597 Table 1: Comparison of the measured and simulated evolution of the surface area of C_3S per 1 g anhydrous material
598 during hydration. The aqueous phase composition is additionally shown.

599 In view of the quantitative comparison in Table 1, the reaction zone hypothesis enables to
600 simulate the measured (HXCT and NF-PXCT) development of the C_3S particle sizes during
601 hydration (at least for the samples analysed in this study). Therefore, to predict the surface
602 area of C_3S during hydration, the starting particle size distribution and the degree of hydration
603 of the bulk sample are sufficient as input parameters for equations (3) – (6). These reported
604 values can be used, for example, as parameters for the simulation of the C_3S hydration kinetics
605 during the first 24 h of hydration. For this purpose, Table 1 summarizes additionally the values
606 obtained in the current study regarding the aqueous phase composition and related simulated

surface area of C_3S for the samples hydrated for 4 h, 8 h, 12 h and 16 h with respect to 1 g alite at 0 h. An integration of our results into kinetic models and the discussion of basic mechanisms for C_3S hydration in the light of our data is beyond the scope of this paper.

The reaction zone hypothesis was applied here for the computation of C_3S layer dissolved during hydration and showed good agreement with the experimental data for the evolution of the C_3S particle size distribution during hydration. In addition to this, the reaction zone hypothesis can be applied to the thickness of the C-S-H layer formed around the C_3S particles during hydration as originally proposed [8, 56, 57]. However, the evaluation of such a model would require the extraction of the C-S-H rim thickness from the nano-tomography data which has not been successfully realized. It was also attempted to obtain information on the thickness of the hydrated rim from the SEM data but the uncertainty in the C-S-H shell thickness results obtained by this method was too high. This has prevented an evaluation of the reaction zone hypothesis to the C-S-H layer and such an extension can be the scope of future studies.

5. Conclusions

The present study focuses on the measurement of the time-dependent C_3S particle size distribution during the main hydration period of C_3S. Since the C_3S particles are overgrown by C-S-H, phase selective synchrotron radiation nano-tomography was applied for the first time to cementitious materials by combining two different operation modes (HXCT and NF-PXCT). The obtained volume distribution of C_3S particles shows good accordance between HXCT and NF-PXCT results. The experimental data indicate that the C_3S particles sizes decrease during hydration, which leads to a decrease of the specific surface area of C_3S due to the consumption of small particles.

The obtained experimental results are used to simulate the process of C_3S dissolution during hydration using a constant reacted rim thickness for all C_3S particle sizes that varies with the degree of hydration ('reaction zone hypothesis' [8]). For this purpose, the degree of hydration of the bulk samples and the C_3S particle size distribution of the starting material are used as input parameters for these simulations. The degree of hydration during the first 20 hours of hydration was independently determined by means of QXRD, ^{29}Si MAS NMR, and TA with consistent results. The simulation of the C_3S particle size distribution based on the "reaction zone hypothesis" showed good agreement with the measured values by HXCT and NF-PXCT for our samples. It has to be noted that only particles bigger than 124 nm in diameter are investigated and compared to calculated values. Thus, the 'reaction zone hypothesis' appears to be an adequate description of the development of the particle size distribution of C_3S during hydration.

Acknowledgements

This work was supported by the European Synchrotron Research Facility under the project number CH 5449 "Surface area of hydrated cement calculated from SR nano-tomography" to F. Bellmann.

References

1. Taylor, H.F.W., *Cement Chemistry*. 2nd ed. 1997: Thomas Telford, London.
2. Ouzia, A. and K. Scrivener, *The needle model: A new model for the main hydration peak of alite.* Cement and Concrete Research, 2019. **115**: p. 339-360.
3. Rößler, C., F. Steiniger, and H.-M. Ludwig, *Characterization of C–S–H and C–A–S–H phases by electron microscopy imaging, diffraction, and energy dispersive X-ray spectroscopy.* Journal of the American Ceramic Society, 2017. **100**(4): p. 1733-1742.
4. Möser, B. and J. Stark, *A New Model Of Ordinary Portland Cement Hydration Derived By Means Of ESEM-FEG*. Materials Science of Concrete: Cement and Concrete - Trends and Challenges, ed. A.J. Boyd, S. Mindess, and J.P. Skalny. 2002: Wiley.
5. Gartner, E.M., et al., eds. *Hydration of Portland Cement*. Structure and Performance of Cements, ed. J. Bensted and P. Barnes. 2002. 57-113.
6. Garrault, S., et al., *Study of C-S-H growth on C3S surface during its early hydration.* Materials and Structures, 2005. **38**(4): p. 435-442.
7. Kjellsen, K.O. and H. Justnes, *Revisiting the microstructure of hydrated tricalcium silicate– – a comparison to Portland cement.* Cement and Concrete Composites, 2004. **26**(8): p. 947-956.
8. Masoero, E., J.J. Thomas, and H.M. Jennings, *A Reaction Zone Hypothesis for the Effects of Particle Size and Water-to-Cement Ratio on the Early Hydration Kinetics of C3S.* Journal of the American Ceramic Society, 2014. **97**(3): p. 967-975.
9. Bergold, S.T., F. Goetz-Neunhoeffer, and J. Neubauer, *Mechanically activated alite: New insights into alite hydration.* Cement and Concrete Research, 2015. **76**: p. 202-211.
10. Song, Y., et al., *Pore network of cement hydrates in a High Performance Concrete by 3D FIB/SEM – Implications for macroscopic fluid transport.* Cement and Concrete Research, 2018.
11. da Silva, Í.B., *X-ray Computed Microtomography technique applied for cementitious materials: A review.* Micron, 2018. **107**: p. 1-8.
12. Aranda, M.A.G., *Recent studies of cements and concretes by synchrotron radiation crystallographic and congnate methods.* Crystallography Reviews, 2015. **22**(3): p. 150-196.
13. Stampanoni, M., et al., *Coherent X-ray Imaging: Bridging the Gap between Atomic and Micro-scale Investigations.* CHIMIA International Journal for Chemistry, 2014. **68**(1): p. 66-72.
14. Parisatto, M., et al., *Examining microstructural evolution of Portland cements by in-situ synchrotron micro-tomography.* Journal of Materials Science, 2015. **50**(4): p. 1805-1817.
15. Cuberos, A.J.M., et al., *Phase development in conventional and active belite cement pastes by Rietveld analysis and chemical constraints.* Cement and Concrete Research, 2009. **39**(10): p. 833-842.
16. Álvarez-Pinazo, G., et al., *In-situ early-age hydration study of sulfobelite cements by synchrotron powder diffraction.* Cement and Concrete Research, 2014. **56**(0): p. 12-19.
17. Artioli, G., *Powder Diffraction and Synchrotron Radiation*, in *Synchrotron Radiation: Basics, Methods and Applications*, S. Mobilio, F. Boscherini, and C. Meneghini, Editors. 2014, Springer Berlin Heidelberg.
18. De La Torre, Á.G., et al., *The superstructure of C3S from synchrotron and neutron powder diffraction and its role in quantitative phase analyses.* Cement and Concrete Research, 2002. **32**(9): p. 1347-1356.
19. Garbev, K., et al., *Cell Dimensions and Composition of Nanocrystalline Calcium Silicate Hydrate Solid Solutions. Part 1: Synchrotron-Based X-Ray Diffraction.* Journal of the American Ceramic Society, 2008. **91**(9): p. 3005-3014.
20. Merlini, M., et al., *The early hydration and the set of Portland cements: In situ X-ray powder diffraction studies.* Powder Diffraction, 2012. **22**(3): p. 201-208.
21. Schlegel, M.-C., et al., *First Seconds in a Building's Life – In Situ Synchrotron X-Ray Diffraction Study of Cement Hydration on the Millisecond Timescale.* Angewandte Chemie International Edition, 2012. **51**(20): p. 4993-4996.

22. Gutberlet, T., et al., *New insights into water bonding during early tricalcium silicate hydration with quasielastic neutron scattering.* Cement and Concrete Research, 2013. **51**(0): p. 104-108.
23. Chae, S.R., et al., *Advanced Nanoscale Characterization of Cement Based Materials Using X-Ray Synchrotron Radiation: A Review.* International Journal of Concrete Structures and Materials, 2013. **7**(2): p. 95-110.
24. Monteiro, P.J.M., et al., *Characterizing the nano and micro structure of concrete to improve its durability.* Cement and Concrete Composites, 2009. **31**(8): p. 577-584.
25. Provis, J.L., et al., *Nanostructural characterization of geopolymers by advanced beamline techniques.* Cement and Concrete Composites, 2013. **36**: p. 56-64.
26. Brisard, S., M. Serdar, and P.J.M. Monteiro, *Multiscale X-ray tomography of cementitious materials: A review.* Cement and Concrete Research, 2020. **128**: p. 105824.
27. Artioli, G., et al., *Direct Imaging of Nucleation Mechanisms by Synchrotron Diffraction Micro-Tomography: Superplasticizer-Induced Change of C–S–H Nucleation in Cement.* Crystal Growth & Design, 2015. **15**(1): p. 20-23.
28. Stockmar, M., et al., *Near-field ptychography: phase retrieval for inline holography using a structured illumination.* Scientific Reports, 2013. **3**: p. 1927.
29. Monteiro, P.J.M., et al., *Advances in characterizing and understanding the microstructure of cementitious materials.* Cement and Concrete Research, 2019. **124**: p. 105806.
30. Trtik, P., et al., *Density mapping of hardened cement paste using ptychographic X-ray computed tomography.* Cement and Concrete Composites, 2013. **36**: p. 71-77.
31. da Silva, J.C., et al., *Mass Density and Water Content of Saturated Never-Dried Calcium Silicate Hydrates.* Langmuir, 2015. **31**(13): p. 3779-3783.
32. Cuesta, A., et al., *Quantitative disentanglement of nanocrystalline phases in cement pastes by synchrotron ptychographic X-ray tomography.* International Union of Crystallography Journal, 2019. **6**(3): p. 473-491.
33. Cuesta, A., et al., *Chemistry and Mass Density of Aluminum Hydroxide Gel in Eco-Cements by Ptychographic X-ray Computed Tomography.* The Journal of Physical Chemistry C, 2017. **121**(5): p. 3044-3054.
34. Cuesta, A., et al. *In situ hydration imaging study of a ye'elimite paste by ptychographic x-ray computed tomography*. in *39th International Conference on Cement Microscopy ICMA*. 2017.
35. Geng, G., et al., *Synchrotron X-ray nanotomographic and spectromicroscopic study of the tricalcium aluminate hydration in the presence of gypsum.* Cement and Concrete Research, 2018. **111**: p. 130-137.
36. Garrault, S., T. Behr, and A. Nonat, *Formation of the C-S-H Layer during Early Hydration of Tricalcium Silicate Grains with Different Sizes.* The Journal of Physical Chemistry B, 2006. **110**(1): p. 270-275.
37. Franke, B., *Bestimmung von Calciumoxyd und Calciumhydroxyd neben wasserfreiem und wasserhaltigem Calciumsilikat.* Zeitschrift für anorganische und allgemeine Chemie, 1941. **247**(1-2): p. 180-184.
38. Sowoidnich, T., et al., *Calcium complexation and cluster formation as principal modes of action of polymers used as superplasticizer in cement systems.* Cement and Concrete Research, 2015. **73**(0): p. 42-50.
39. Jiang, S.P., J.C. Mutin, and A. Nonat, *Studies on mechanism and physico-chemical parameters at the origin of the cement setting II. Physico-chemical parameters determining the coagulation process.* Cement and Concrete Research, 1996. **26**(3): p. 491-500.
40. Jönsson, B., et al., *Controlling the Cohesion of Cement Paste.* Langmuir, 2005. **21**(20): p. 9211-9221.
41. Kong, X., et al., *Retardation effect of styrene-acrylate copolymer latexes on cement hydration.* Cement and Concrete Research, 2015. **75**: p. 23-41.
42. O'Connor, B.H. and M.D. Raven, *Application of the Rietveld Refinement Procedure in Assaying Powdered Mixtures.* Powder Diffraction, 2013. **3**(1): p. 2-6.

43. Jansen, D., et al., *A remastered external standard method applied to the quantification of early OPC hydration.* Cement and Concrete Research, 2011. **41**(6): p. 602-608.
44. Golovastikov, N.I., *Crystal Structure of Tricalcium Silicate, 3CaOSiO2 = C3S.* Sov. Phys. Crystallogr., 1975. **20**: p. 441-445.
45. Busing, W.R. and H.A. Levy, *Neutron Diffraction Study of Calcium Hydroxide.* The Journal of Chemical Physics, 1957. **26**(3): p. 563-568.
46. Bergold, S.T., F. Goetz-Neunhoeffer, and J. Neubauer, *Quantitative analysis of C–S–H in hydrating alite pastes by in-situ XRD.* Cement and Concrete Research, 2013. **53**: p. 119-126.
47. Bellmann, F., et al., *Improved evidence for the existence of an intermediate phase during hydration of tricalcium silicate.* Cement and Concrete Research, 2010. **40**(6): p. 875-884.
48. Sowoidnich, T., et al., *New insights into tricalcium silicate hydration in paste.* Journal of the American Ceramic Society, 2019. **102**(5): p. 2965-2976.
49. Massiot, D., et al., *Modelling one- and two-dimensional solid-state NMR spectra.* Magnetic Resonance in Chemistry, 2002. **40**(1): p. 70-76.
50. Cesar da Silva, J., et al., *Efficient concentration of high-energy x-rays for diffraction-limited imaging resolution.* Optica, 2017. **4**(5): p. 492-495.
51. Barret, P. and D. Bertrandie, *Fundamental hydration kinetic features of the major cement constituents: Ca[3]SiO[5] and beta Ca[2]SiO[4].* Journal de chimie physique, 1986. **83**(11-12): p. 765-775.
52. Haas, J. and A. Nonat, *From C–S–H to C–A–S–H: Experimental study and thermodynamic modelling.* Cement and Concrete Research, 2015. **68**(0): p. 124-138.

53. Stark, J. and B. Wicht, Zement und Kalk: Der Baustoff Als Werkstoff, 2000: Birkhauser Verlag GmbH.
54. Exner, H.E.: Stereology and 3D Microscopy: Useful Alternatives or Competitors in the Quantitative Analysis of Microstructures? 2004. 23(2): p. 73-82.
55. Neerad Phansalkar, Sumit More, Ashish Sabale and Madhuri Joshi, "Adaptive local thresholding for detection of nuclei in diversity stained cytology images," *2011 International Conference on Communications and Signal Processing*, Kerala, India, 2011, pp. 218-220.
56. J.J. Biernacki, T. Xie, Advanced single particle model for C3S and alite hydration, J. Am. Ceram. Soc. 94 (7) (2011) 2037–2047.
57. T. Honorio, B. Bary, F. Benboudjema, S. Poyet, Modeling hydration kinetics based on boundary nucleation and space-filling growth in a fixed confined zone, Cem. Concr. Res. 83 (2016) 31–44.
58. C. Naber, F. Bellmann, J. Neubauer, Influence of w/s ratio on alite dissolution and C-S-H precipitation rates during hydration, Cem Concr Res 134 (2020) 106087.
59. A. Zingg, L. Holzer, A. Kaech, F. Winnefeld, J. Pakusch, S. Becker, L. Gauckler, The microstructure of dispersed and non-dispersed fresh cement pastes -- New insight by cryo-microscopy, Cem. Concr. Res., 38 (2008) 522-529.
60. L. Holzer, P. Gasser, A. Kaech, M. Wegmann, A. Zingg, R. Wepf, B. Muench, Cryo-FIB-nanotomography for quantitative analysis of particle structures in cement suspensions, Journal of Microscopy, 227 (2007) 216-228.
61. F. Kleiner, C. Rößler, F. Vogt, A. Osburg, & H.M. Ludwig, (2021). Reconstruction of calcium silicate hydrates using multiple 2D and 3D imaging techniques: Light Microscopy, µ-CT, SEM, FIB-nT combined with EDX. Journal of Microscopy.